Artigo

Application of SEBAL and T_s/VI Trapezoid Models for Estimating Actual Evapotranspiration in the Algerian Semi-Arid Environment to Improve Agricultural Water Management

Fellah Sahnoun[1], Hamimed Abderrahmane[1] (iD), Miloudi Kaddour[1], Khaldi Abdelkader[1],
Benslimane Mohamed[1], Teixeira Antônio Heriberto de Castro[2]

[1]*Biological Systems and Geomatics Laboratory, University Mustapha Stambouli of Mascara, Algeria.*
[2]*Water Resources Department, Universidade Federal de Sergipe, Aracaju, SE, Brazil.*

Abstract

Accurate spatio-temporal estimation of evapotranspiration (ET) and surface energy fluxes is crucial for many agro-environmental applications, including the determination of water balance, irrigation scheduling, agro-ecological zoning, simulation of global changes in land use and forecasting crop yields. Remote sensing based energy balance models are presently most suitable for estimating ET at both temporal and spatial scales. This study presents an intercomparison of ET maps over the Habra plain in western Algeria obtained with two different models: T_s/VI trapezoid (Surface temperature/Vegetation Index Trapezoid Model) and SEBAL (Surface Energy Balance Algorithm for Land). T_s/VI trapezoid is the most used model, due to its simplicity, ease of use, few data input requirements and relatively high accuracy. It allows estimating ET directly by using the Priestley-Taylor equation. Whereas SEBAL allows estimating ET as the residual term of the energy balance equation, by using a rather complex hot and cold pixel based contextual approach to internally calibrate sensible heat flux through an iterative approach. The data set consists of four Landsat-8 OLI/TIRS images acquired on 2018-2019 and some ground measurements. In conclusion, the results show that SEBAL and T_s/VI trapezoid models provide comparable outputs and suggest that both the two models are suitable approaches for ET mapping over agricultural areas where ground measurements are scarce or difficult to collect.

Keywords evapotranspiration, T_s/VI trapezoid, SEBAL, energy balance, Landsat, Algeria.

Aplicação de SEBAL e T_s/VI Trapézio Modelos para Estimar a Evapotranspiração Real no Ambiente do Argelino Semi-Árido para Melhorar a Gestão da Água na Agricultura

Resumo

Estimativas precisas da evapotranspiração (ET) e dos fluxos de energia na superfície são cruciais para muitas aplicações agro ambientais, incluindo a determinação do balanço hídrico, manejo da irrigação, zoneamentos agro ecológicos, simulações de mudanças globais no uso da terra e previsão da produção de culturas agrícolas. Modelos de balanço de energia por sensoriamento remoto são atualmente os mais indicados para estimativa da ET em ambas as escalas, temporal e espacial. Este estudo apresenta inter comparações de mapas da ET para a planície Mascara (oeste da Argélia) obtidos com dois diferentes modelos: trapezoidal T_s/VI (Surface temperature/Vegetation Index Trapezoid Model) e o SEBAL (Surface Energy Balance Algorithm for Land). O método T_s/VI trapezoid é o mais usado, devido à sua simplicidade, fácil uso, requerimento de poucos dados de entrada e precisão relativamente alta. Ele permite a estimativa da ET diretamente através do uso da equação de Priestley-Taylor. Enquanto que SEBAL permite a estimativa da ET como um termo residual na equação do balanço de energia, usando um processo muito complexo de determinação de pixels quente e frio para calibração interna do fluxo de calor sensível por um método iterativo. A série de dados consistiu de quatro imagens Landsat-8 OLI/TIRS adquidasem 28 de setembro de 2018, 2 de janeiro de 2019, 8 de abril de 2019 e

Corresponding author: Hamimed Abderrahmane, hamimed@univ-mascara.dz.

10 de maio de 2019 e algumas medições agrometeorológicas em campo. Os modelos SEBAL e T$_s$/VI trapezoid apresentaram resultados similares, concluindo-se que ambos são viáveis para estimativa da ET em áreas agrícolas nas condições de medições de campo escassas ou de difícil obtenção.

Palavras-chave evapotranspiração, T$_s$/VI trapezoid, SEBAL, balanço de energia, Landsat, Argélia.

1. Introduction

The spatio-temporal estimation of evapotranspiration (ET) from agricultural regions is important for agriculture water management, especially in arid and semiarid regions where water deficiency is becoming a major constraint for economic development (Yang *et al.*, 2019). Conventional methods (such as Bowen ratio system, eddy covariance system, or weighting lysimeters) that use point measurements to estimate ET are representative only of local areas and cannot be extended to large areas because of heterogeneity of landscape (Liu and Xu, 2019). Remote sensing-based energy balance models are presently best alternatives for estimating ET at both field and regional scales where ground measurements are not feasible and reliable estimates of ET are needed (Yang *et al.*, 2019; Zhang *et al.*, 2016).

The ET is a major component of the terrestrial hydrological cycle, nearly two-thirds of precipitation over land is returned back to the atmosphere by ET (Brutsaert, 2013). This proportion may be higher in dry regions, such as the Mediterranean basin (Boulet *et al.*, 2020). Inaccurate estimates of ET in these regions can cause large errors in the hydrological components prediction such as runoff and recharge, and in the associated water balance and water resources availability (Zhang *et al.*, 2017).

Remote sensing technology facilitates the calculation of albedo, vegetation indexes and surface temperature, which are necessary to remote sensing-based energy balance models for scaling up ET and surface energy fluxes to larger spatial and longer temporal scales (Chen and Liu, 2020). To this end, major effort has been devoted over the past three decades to improve remote sensing-based methods that provide spatially distributed surface fluxes maps using airborne and satellite data (Nehal *et al.*, 2017). These methods can be classified into three main categories: a) Methods using simple empirical relationships relating daily ET to an instantaneous surface temperature measurement (Trezza *et al.*, 2013; Huang *et al.*, 2019); 2) Methods using deterministic relationships based on more complex models such as Soil-Vegetation-Atmosphere Transfer models (SVAT) (Olioso *et al.*, 2005; Chebbi *et al.*, 2018; Bigeard *et al.*, 2019); 3) Methods based on ET estimation as the residual term of the energy balance equation, which can be divided into two categories:

1) Single-source models, such as SEBAL (Surface Energy Balance Algorithm for Land) (Bastiaanssen *et al.*, 1998; Bastiaanssen *et al.*, 2005), METRIC (Mapping Evapotranspiration with Internalized Calibration) (Allen *et al.*, 2007; Ramírez-Cuesta *et al.*, 2020), T$_s$/VI trapezoid model

(Jiang and Islam, 2001; Stisen *et al.*, 2008; Zhu *et al.*, 2017), SEBS (Surface Energy Balance System) (Su, 2002; Chen *et al.*, 2019), S-SEBI (Simplified Surface Energy Balance Index) (Roerink et al, 2000; Allies *et al.*, 2020), that do not distinguish between soil evaporation and transpiration. Their simplicity has made the single-source models widely used; 2) dual-source models, such as TSEB (Two Source Energy Balance) (Kustas *et al.*, 2018), ALEXI or Dis-ALEXI (Anderson *et al.*, 2007) and SPARSE (Soil Plant Atmosphere and Remote Sensing Evapotranspiration) (Boulet *et al.*, 2018) that discriminates the soil and vegetation component.

This study evaluates the performance of T$_s$/VI trapezoid and SEBAL models for ET estimation by using four images acquired by Landsat-8 OLI/TIRS. This later provides updated images at 30-m resolution every 16 days. The estimates of these models are then compared with ground observations on barley and artichoke crops using the Bowen Ratio Energy Balance (BREB) method. T$_s$/VI trapezoid model allows estimating ET directly by using the Priestley-Taylor equation, without the need to calculate the sensible heat flux. It requires few input data. It is based on a graphical method in which the extreme values of surface temperature are deduced from the scatterplot between vegetation index (*NDVI*) and surface temperature, and then the Priestley-Taylor parameter is calculated (Stisen *et al.*, 2008). However SEBAL follows an energy balance approach, where the latent heat flux (corresponding to the energetic equivalent of ET) is estimated as the residual term when net radiation, sensible and soil heat fluxes are known, by using a rather complex hot and cold pixel based contextual approach to internally calibrate sensible heat flux through an iterative approach. SEBAL may not be as applicable as other models for ET spatialization over agricultural areas where ground information is scarce or difficult to collect (Khaldi *et al.*, 2011). Moreover, SEBAL has the particularity of using a calibration procedure to compensate for temperature and albedo errors without the need for a complex atmospheric correction (Bastiaanssen *et al.*, 2005).

The goal of this study is to use SEBAL and T$_s$/VI trapezoid models for estimating the actual ET over the agricultural plain of Habra, a semi-arid region with heterogeneous surface conditions in northwestern Algeria, where ground data are scarce or difficult to collect. The region contains extremes in surface albedo, vegetation cover and surface temperature, due to a varied land cover types including irrigated agriculture, rainfed agriculture, bare soil and livestock grazing. The irrigated agriculture in the area is now facing a significant threat, due to limited

water supplies, climate change and an increase in extreme events (Benzater *et al.*, 2021), which appeals us to develop water-saving irrigation for sustainable water use. To this end, a remote sensing approach is required to be routinely applied as a tool for providing both historical and near-real time ET and surface energy fluxes for performing a better management of the agricultural water resources of the area.

2. Study area and used data

2.1. Study area description

The study area corresponds to the agricultural plain of Habra, which houses the irrigation perimeter of Mohammadia. It is located in northwestern Algeria (Oran) between longitudes 0°6'44" W and 0°6'33" E and latitude 35°32'45" N and 35°41'33" N. It covers an area of 328 km² (Fig. 1).

The selected area is part of the great interior plain of Macta, which is the receptacle of the second watershed of Algeria by its area (14500 km²) and only communicates with the Mediterranean Sea by a narrow channel (Benzater *et al.*, 2019). The average altitude is about 40 m.

The soils in the plain of Habra are sedimentary formation with variable texture intake alluvial and alluvio-colluvial. They are distributed in the plain into entities more or less uniform and regular. Soil salinity is between 8 and 16 mS/cm at depth of more than 50 cm with low rate of leaching.

The climate in the study region is Mediterranean semi-arid with mild winter. Two main periods characterized this region, a rainy period during the months of autumn (September, October and November), winter (December, January and February) and early spring (March and April), and a dry and hot period during the months of summer (June, July and August). The absolute

minimum air temperature during winter down to 6 to 8 °C. Summer is usually dry and warm. The absolute maximum air temperature is equal to 42 °C. The average annual rainfall for the period 1970-2011 is about 450 mm (Elouissi *et al.*, 2017).

The rural areas with rich soils are suitable for agriculture but where the soils are poor, livestock grazing (rangelands) is dominant. Irrigated agriculture is dominant in the study area and the main crops include fruits mainly citrus and garden crops such as artichoke. Rainfed agriculture occupies a small part and the main crops include cereals mainly barley (Fig. 2).

The irrigation perimeter of Mohammadia is relatively old, dating back to 1940. It covers an area equipped for irrigation (irrigable area) of about 19630 ha (the total area is about 21210 ha), predominantly arboreal and particularly citrus. It is considered the most important in Algeria northwestern. Despite this, few studies on the management of its irrigation water were performed (Tazekrit *et al.*, 2017). Irrigation water is conveyed to the irrigation perimeter through a classical irrigation network from three dam reservoirs, namely Fergoug, Bouhanifia and Ouizert, which operate in cascade. This water knows significant losses during transfer, due to illegal consumption along the stream. The irrigation network is of the gravity type, with open channels of trapezoidal or circular shape totaling a length of 256 km (Zerkaoui *et al.*, 2017). Its management is provided by the national office for irrigation and drainage in consultation with the association of irrigators. So far, this network is the only way to supply the irrigation water to the majority of irrigated crops because groundwater in the area is brackish and cannot be used to irrigate citrus orchards (Tazekrit *et al.*, 2017).

In the early 1960s, the irrigation perimeter received a total water volume of about 80 million m³/year. This volume has been constantly decreasing since 1977 and the irrigation quotas allocated for all irrigable area did not
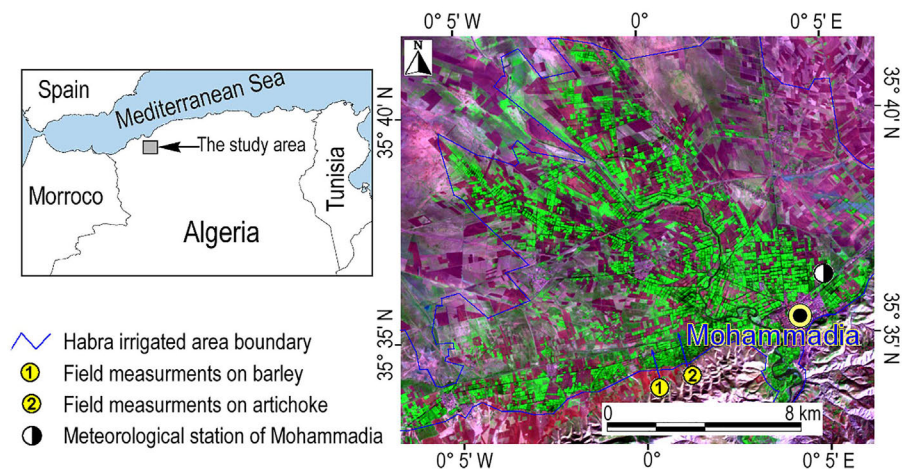

Figure 1 - Location and false color composite 4,3,2 of Landsat-8 OLI/TIRS imagery acquired on 2 January 2019 (DOY 2) of the study site over the Habra plain, Algeria.
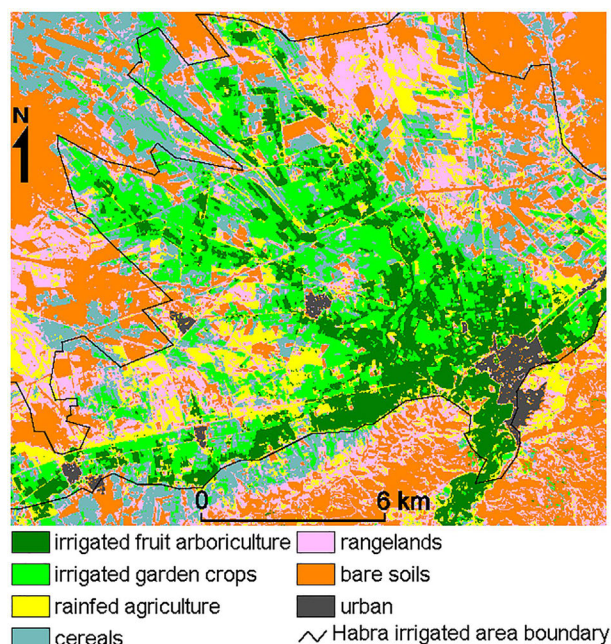
Figure 2 - Land use map in the study area (Habra plain).

exceed 32 million m³/year. This reduction is due to the lack of water resources caused by recurrent drought plaguing Algeria's western region for two decades (1977-1997) and by allocating water as a priority for domestic use (Sutton and Zaimeche, 1992).Over the past decade, the allocated irrigation water volumes are still weak and have

little exceeded 26 million m³. Such a situation of water resources cannot meet the survival needs of orchards, which has led to the decline of several hundred hectares of trees and the reduction of irrigated area to about 50% (Zerkaoui, 2017).

2.2. The used data

Remote sensing data used in this work consists of four Landsat-8 OLI/TIRS images acquired during 2018 and 2019 (Table 1). They are freely downloadable https:// earthexplorer.usgs.gov.

Remote sensing data are supplemented by ground measurements which were performed on two points located in the experimental site of the National Institute of Plant Protection in Mohammadia city. The first point was located on barley crop and the second on artichoke crop (Fig. 1). These measurements were intended for the daily monitoring of energy fluxes at the soil-plant-atmosphere continuum. They correspond to the radiometric surface temperature, the reflected radiation and the three components of surface energy balance, i.e. soil heat flux, sensible heat flux and latent heat flux. Incoming shortwave (solar) and thermal radiations were measured on the meteorological station of Mohammadia (ONM), located in the study area (Fig. 1) using a pyranometer and a pyrgeometer, respectively. The meteorological station also provided measurements on the reference variables which are air temperature, air humidity, wind speed, air pressure, sunshine duration and daily potential ET (Table 2). On the experimental device, installed on the plots of barley and artichoke, the albedo was obtained from the ratio of the reflected radiation (measured by an Apogee pyranometer (model MP-200)) and the incoming shortwave radiation. The net radiation is determined from the radiative balance equation, depending on the albedo, the incoming shortwave and thermal radiations and the surface emission which is deduced from the radiometric surface temperature. The latter is measured by an Apogee infrared radiometer (IRTS-P model). The soil heat flux is measured

Table 1 - Landsat 8-OLI imagery used in the study.

(Path/ Row)	Acquisition Date	Acquisition moment (GMT)	Day of the year(DOY)	Solar elevation (degree)
198/35	28/09/2018	10h38′	271	46.8
198/35	02/01/2019	10h38′	2	28.3
197/35	16/03/2019	10h31′	75	46.7
198/35	10/05/2019	10h37′	130	64.2

Table 2 - Meteorological conditions during the image acquisition of Landsat 8-OLI/TIRS on the selected days.

Parameter	Unit	28/09/2018 (DOY 271)	02/01/2019 (DOY 2)	16/03/2019 (DOY 75)	10/05/2019 (DOY 130)
Air Temperature	°C	25	14.4	21.2	21.5
Relative humidity	%	57.5	44.5	25.1	58.5
Atmospheric Pressure	mbar	1013.23	1023.02	1016.3	1009.8
Incoming shortwave radiation	W/m²	720.5	472.2	767.8	913.6
Atmospheric radiation	W/m²	372.7	284.5	304.9	346.4
Atmospheric transmittance	–	0.72	0.70	0.76	0.75
Wind speed	m/s	1.5	2.2	1.8	1.2
Relative sunshine duration	–	0.82	0.63	0.68	0.71
Potential evapotranspiration	mm	3.94	0.82	3.76	5.53

using three Hukseflux conductive flux plates (HFP01SC model) installed at 5 cm depth in the soil. Sensible and latent heat fluxes were computed from measurements at two levels (0.5 and 2.5 m above the surface) of air temperature and relative humidity using the BREB technique.

3. Models description

3.1. Surface Energy Balance Algorithm for Land (SEBAL) model

The following presents a brief description of SE-BAL, with further details found in Bastiaanssen *et al.* (1998) and Bastiaanssen *et al.* (2005). SEBAL is a remote sensing processing model for estimating instantaneous terms of the energy balance equation, including ET flux, at the satellite overpass time.

For the determination of ET, SEBAL estimates the latent heat flux (λE) as the residual term of the energy balance equation which describes the energy exchange between the land surface and the atmosphere:

$$\lambda E = Rn - G - H \quad (1)$$

where Rn is the net radiation at the surface (W/m^2), H is the sensible heat flux (W/m^2), G is the soil heat flux (W/m^2) and λE is the latent heat flux (energy consumed by ET, W/m^2) (Table 3). Net radiation (Rn) estimation is quite similar for both models; it is calculated according to:

$$Rn = (1 - r_0) \cdot Rg + L^{\downarrow} - L^{\uparrow} \quad (2)$$

where Rg is the incoming shortwave radiation, partly reflected depending on the albedo r_0, $L^{\downarrow}$ and $L^{\uparrow}$ are the incoming and the emitted outgoing longwave radiations (W/m^2), respectively.

Mapping the net radiation (Rn) requires evaluation of 1) the incoming shortwave radiation (Rg) which is obtained from the weather observations. It allowed us to estimate the atmospheric transmittance (which represents the capacity of the atmosphere to transmit solar radiation), 2) the outgoing longwave radiations ($L^{\uparrow}$), obtained by the expression of Stephan-Boltzmann, using surface temperature and surface emissivity and 3) the incoming longwave radiation ($L^{\downarrow}$), using air temperature and atmosphere emissivity (ε_a). This latter is calculated depending on atmospheric transmittance (τ) following the expression (Bastiaanssen *et al.*, 1998):

$$\varepsilon_a = 1.08 \times (- \ln \tau)^{0.265} \quad (3)$$

The soil heat flux (G) cannot be directly determined from satellite sensors and requires an empirical formulation. It has been estimated as a fraction of Rn with the coefficient a function of surface temperature, albedo and vegetation index (Bastiaanssen *et al.*, 2000):

Table 3 - List of symbols used in this study.

Symbol	Unit	Description
$L^{\downarrow}$	W/m^2	incomingoutgoing longwave radiations
$L^{\uparrow}$	W/m^2	emitted outgoing longwave radiations
Rg	W/m^2	incoming shortwave radiation
Rn	W/m^2	net radiation at the surface
G	W/m^2	soil heat flux
λE	W/m^2	latent heat flux
ET_{hor}	mm/h	hourly latent heat flux
EF	W/m^2	evaporative fraction
T_0	K	radiometric surface temperature
T_a	K	air temperature
T_{aero}	K	aerodynamic temperature
dT	K	near-surface temperature difference
ρ	kg/m^3	Air density
Cp	J/kg/K	Air specific heat at constant pressure
r_{ah}	s/m	aerodynamic resistance to heat transport
λ	J/kg	latent heat of vaporization of water
γ	Mbar/K	psychrometric constant
Δ	mbar.K	slope of the saturation vapor curve
σ	W/(m^{2}K^4)	The Bolzman constant
r_s	s/m	surface resistance to evaporation
φ	–	Priestley-Taylor parameter
f_c	–	fraction cover
ε_a	–	Atmosphere emissivity
ε_0	–	Surface emissivity
τ	–	Atmospheric transmittance
r_0	–	Surface albedo
$NDVI$	–	normalized difference vegetation index
k	–	von Karman's constant (=0.41)
u^*	m/s	friction velocity
u_{200}	m/s	wind speed at blending height (200 m)
g	m/s^2	acceleration due to gravity
L	m	Monin-Obukhov length
z_{om}	m	roughness length for momentum transport
ψ_h	–	stability function for heat transport
ψ_m	–	stability function for momentum transport

$$\frac{G}{Rn} = T_0(0.0038 + 0.0074\ r_0) \times (1 - 0.978\ NDVI^4) \quad (4)$$

The sensible heat flux (H) is expressed as a function of the near-surface air temperature difference (T_{aero} - T_a) as follows:

$$H = \frac{\rho \cdot Cp}{r_{ah}}(T_{aero} - T_a) \quad (5)$$

where ρ is air density (kg/m^3), Cp is air specific heat at constant pressure (J/kg/K), r_{ah} is the aerodynamic resis-

tance to heat transfer, T_{aero} is the aerodynamic temperature (K) and T_a is the air temperature (K). In satellite remote sensing applications, the radiometric surface temperature (T_0) retrieval is often used instead of the aerodynamic temperature (T_{aero}) in Eq. (5) (Kustas *et al.*, 1989).

In SEBAL, the sensible heat flux (H) is estimated by using the following expression:

$$H = \frac{\rho \cdot Cp}{r_{ah}} dT \qquad (6)$$

where dT is the near-surface temperature difference between two near surface heights $z_1= 0.1$ m and $z_2= 2$ m above the canopy layer, and r_{ah} is the aerodynamic resistance to heat transport between these levels (s/m). dT is used in Eq. (6) because of the difficulty in estimating surface temperature T_0 accurately from satellite due to uncertainty in atmospheric attenuation or contamination and radiometric calibration of the sensor (Allen *et al.*, 2007). In addition, T_0, as measured by satellite (i.e., radiometric or kinetic temperature) can deviate from the "aerodynamic" temperature that drives the heat transfer process by several degrees (Qualls and Brutsaert, 1996).

In this model, the difference dT between the two near surface heights 0.1 and 2 m is approximated by a simple linear function:

$$dT = a \cdot T_0 + b \qquad (7)$$

The coefficients a and b in Eq. (7) are empirically determined using the properties of pixels in extreme water conditions (hot/cold and dry/wet). These pixels are identified on the image by analyzing the vegetation index and the surface temperature relationship according to the trapezoid method (Hamimed *et al.*, 2014). The dry pixels are indicated at bare soils (*NDVI* values close to zero) having high surface temperature. However, the wet pixels are indicated at fully vegetation (*NDVI* > 0.7) having low surface temperature. The thresholds of low and high temperatures are defined as the equilibrium surface temperatures resulting from the energy balance for well-watered dense vegetation and dry bare soil, respectively (Hamimed *et al.*, 2014).

With the identification of wet and dry pixels, we can estimate H_{wet} and H_{dry} from the energy balance equation as follows:

$$H_{wet} = (Rn - G)_{wet} - \lambda E_{wet} \qquad (8)$$

$$H_{dry} = (Rn - G)_{dry} - \lambda E_{dry} \qquad (9)$$

A dry pixel is characterized by a zero latent heat flux ($\lambda E_{dry} = 0$), which means, the overall available energy $(Rn\text{-}G)_{dry}$ is partitioned into sensible heat flux. For a wet

pixel, the latent heat flux (λE_{wet}) in SEBAL is assumed to be equal to the hourly grass reference ET (ETr), by using Penman-Monteith equation (Allen *et al.*, 1998), multiplied by an empirical coefficient of 1.05. The choice of this coefficient is primarily dictated by assumption that a wet pixel (fully covered by vegetation) usually has an ET value of 5% larger than ETr (Gavilán *et al.*, 2019).

By inverting the Eq. (6), H_{wet} (or H_{dry}) value allows deducing the temperature difference dT_{wet} (or dT_{dry}) between the two near surface heights 0.1 and 2 m. The coefficients a and b of Eq. (7) are determined by fitting a line using dT and T_0 values of both dry and wet pixels in the image.

In SEBAL, r_{ah} is calculated between z_1 and z_2 using a wind speed extrapolated from some blending height above the surface ($\sim$200 m, a height of 200 m was used in this study) and an iterative procedure for correcting atmospheric stabilities to heat and momentum transfer, based on the Monin-Obukhov's similarity theory. For the first estimation of H, the atmospheric condition is assumed to be neutral, and r_{ah} is calculated as:

$$r_{ah} = \frac{\ln(z_2/z_1)}{u* .k} \qquad (10)$$

where k is von Karman's constant (= 0.41) and $u*$ is friction velocity (m/s), calculated using the logarithmic wind profile for neutral atmospheric condition for the first iteration as:

$$u* = \frac{k.u_{200}}{\ln(200/z_{om})} \qquad (11)$$

where u_{200} is wind speed at 200 m (corresponding to blending height) and z_{om} is roughness length for momentum transport (m).

In subsequent iterations, the Monin-Obukhov length (L) is first calculated to examine the stability conditions of the atmosphere:

$$L = -\frac{\rho.Cp.u*^3.T_0}{k.g.H} \qquad (12)$$

where g is the acceleration due to gravity (= 9.81 m/s²).

Then, the corrected values for r_{ah} and $u*$ for each iteration are calculated from Eqs. (13) and (14), respectively, as follows:

$$r_{ah} = \frac{\ln(z_2/z_1) - \psi_h(z_2) + \psi_h(z_1)}{u* .k} \qquad (13)$$

$$u* = \frac{k.u_{200}}{\ln(200/z_{om}) - \psi_m(200)} \qquad (14)$$

where ψ_h (z_2) and ψ_h (z_1) are stability functions for heat transport at heights z_2 and z_1, respectively, and ψ_m (200) is the stability function for momentum transport at blending height (=200m). Both ψ_h and ψ_m are functions of the Monin-Obukhov length, and are computed following Allen *et al.* (2007). The corrected values of r_{ah} and u^* are then used to recalculate H until the value of r_{ah} stabilizes.

Once H is estimated, λE is computed using Eq. (1). This last step leads mapping the latent heat flux. This should help in the interpretation of a surface behaviour with respect to water stress (Bastiaanssen *et al.*, 1998). It is therefore preferable for an easier interpretation to deduce moisture indicators such as the evaporative fraction (*EF*), the surface resistance to evaporation (r_s) and the Priestley-Taylor parameter (α)

The flowchart presented in Fig. 3 summarizes the methodology used in SEBAL model for mapping ET from satellite data and ground measurements.

3.2. Surface temperature/Vegetation Index trapezoid (Ts/VI trapezoid) model

The relationship between surface temperature (T_0, or temperature difference dT_S) and vegetation index (the nor-malized difference vegetation index (*NDVI*)) can be used to describe the evaporative capacity of the land surface assuming that T_0 varies for a given vegetation index mainly depending on the availability of soil moisture rather that differences in atmospheric forcing over a relatively flat area. This relationship has been widely used to obtain information about the energy fluxes or soil moisture of the land surface (Jiang and Islam, 2001; Stisen *et al.*, 2008; Bai *et al.*, 2019). Detailed discussions on the T_0-*NDVI* relation are found in e.g. Sandholt *et al.* (2002), Hu *et al.* (2019), Carlson and Petropoulos (2019) and Carlson (2007). Scatterplots between remotely sensed T_0 and *NDVI* often results in a trapezoidal/triangular shape.

The prerequisite for estimating evaporative fraction (*EF*) and ET from the T_s/VI trapezoid is to determine accurately the lower edge of this space (wet edge) which is characterized by saturated surface soil water content with maximum ET and the upper edge (dry edge) of the scatter plot representing lower limit of surface soil moisture content with limited ET and higher limit of surface temperature for a given *NDVI* (Sandholt *et al.*, 2002). The T_s/VI trapezoid method should ideally be applied over smaller regions and those with little topographic variation (Zhu *et al.*, 2017).
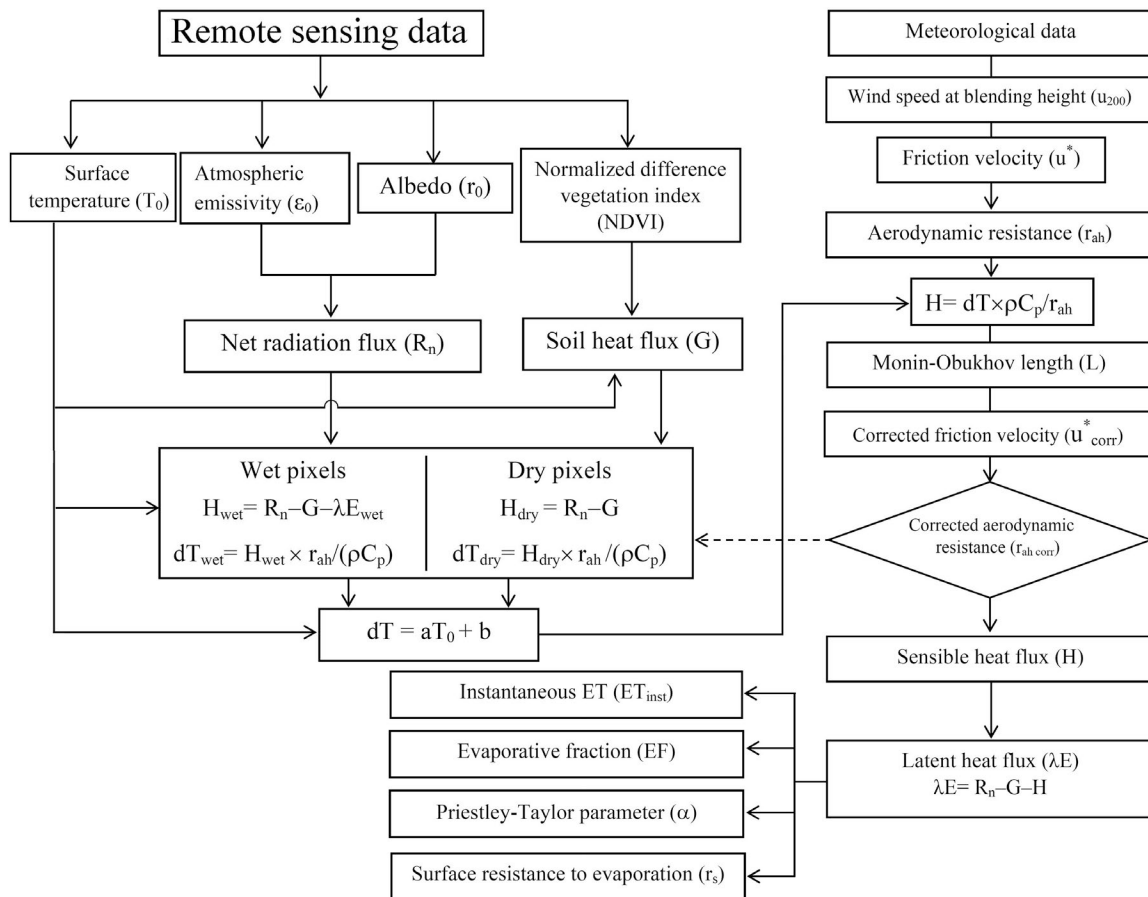

Figure 3 - Flowchart of the methodology used for the spatialization of evapotranspiration and surface energy fluxes with SEBAL model.

The four points of the trapezoid corresponds to extreme conditions of surface in terms of surface temperature and NDVI, which allow deducing the extreme values of surface temperature and *NDVI* (Moran *et al.*, 1994; Hu *et al.*, 2019).

The Priestley-Taylor formulation with fully remotely sensed data proposed by Jiang and Islam (2001) and further improved and validated by Stisen *et al.* (2008) representatively based on the interpretations of the T$_s$/VI trapezoid model, has been employed to estimate ET using the following equation:

$$\lambda E = \varphi \left[(Rn - G) \frac{\Delta}{\Delta + \gamma} \right] \qquad (15)$$

Where *Rn* and *G* are obtained using Eqs. (2) and (4) respectively (both models use the same equations for estimating net radiation and soil heat flux), γ is the psychrometric constant (≈ 0.66 mbar/K) and Δ is the slope of the saturation vapor curve at air temperatures (T_a), calculated with:

$$\Delta = \frac{2503.058}{(T_a + 237.3)^2} \exp \left(\frac{17.27 \, T_a}{T_a + 237.3} \right) \qquad (16)$$

Equation (15) is a modified version of the Priestley-Taylor equation in the case of unsaturated surfaces by the introduction of the parameter φ which represents the so-called Priestley-Taylor parameter, and which accounts for aerodynamic and canopy resistances, and is slightly different from the original Priestley-Taylor's parameter α (≈ 1.26). This parameter depends on surface moisture conditions (Khaldi *et al.*, 2014). It is defined globally to range from $\varphi_{min} = 0$, for a dry bare soil, to $\varphi_{max} = (\Delta + \gamma)/\Delta$, for a saturated or well vegetated surface (Stisen *et al.*, 2008).

As illustrated in Fig. 4, φ_{min} is assigned to a pixel with minimum *NDVI* and maximum temperature; φ_{max} is assigned to pixels with maximum *NDVI*.

φ can be expressed as a function of the evaporative fraction (*EF*) as follows:

$$\varphi = EF \cdot \frac{\Delta + \gamma}{\Delta} \qquad (17)$$

where *EF* is defined as the ratio of ET or latent heat flux (λE) to available energy (*Rn-G*):

$$EF = \frac{\lambda E}{H + \lambda E} = \frac{\lambda E}{Rn - G} = \varphi \frac{\Delta}{\Delta + \gamma} \qquad (18)$$

The parameter φ is estimated following the approach proposed by Jiang and Islam (2001) using three steps (Stisen *et al.*, 2008): In the first step, surface moisture condition is estimated by interpolating the surface temperature between the wet and dry edges. The dry and wet edges are
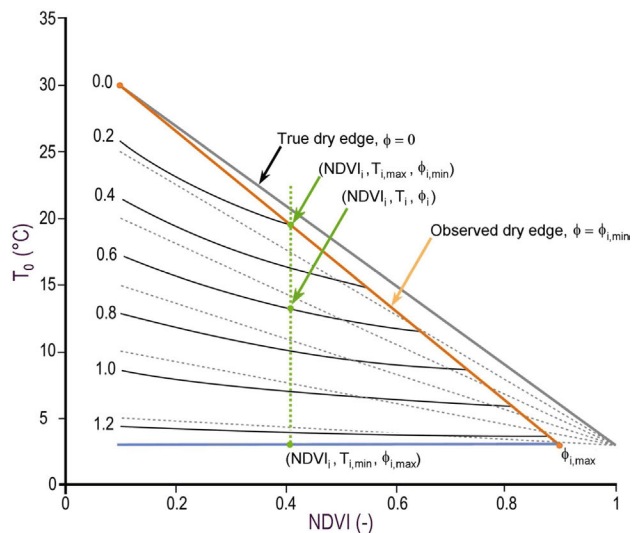

Figure 4 - Illustration of the conceptual T$_s$/NDVI plot. The true dry edge (grey) representing zero ET ($\varphi_{i,min} = 0$), the observed dry edge (red) representing limiting ET ($\varphi_{i,min}$) and the wet edge (blue) representing potential ET (φ_{max}). Dashed grey and solid black lines are iso-lines of equal moisture availability and φ respectively (After Stisen *et al.*, 2008).

experimentally or theoretically identified by determining the surface temperature in the trapezoid corners (Fig. 5) using surface energy balance equation and boundary conditions represented by the surface resistances values for each moisture condition for soil and vegetation. In this study, we set a surface resistance of 10 s/m for wet vegetation cover, 400 s/m for dry vegetation cover, 0 for wet bare soil and ∞ for dry bare soil (Boegh *et al.*, 2002).

In the second step, we estimate $\varphi_{i,min}$ which represents the minimum value of φ for a given fraction cover (f_c) value, as:
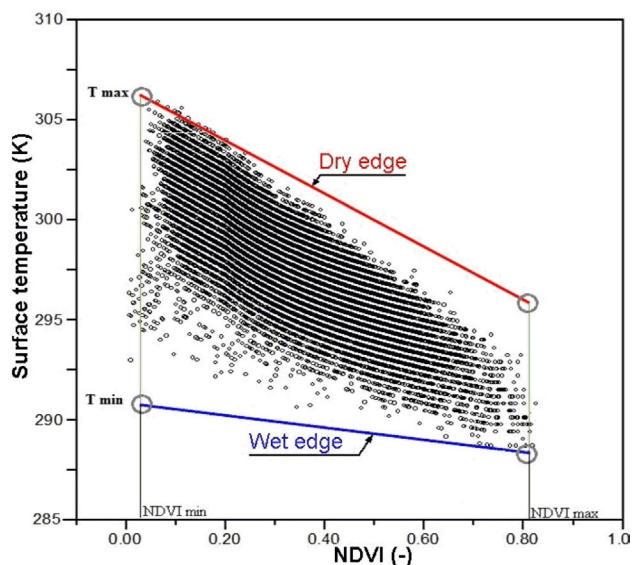

Figure 5 - Illustration of the trapezoid method used for identifying wet and dry pixels (DOY 2).

$$\varphi_{i,\min} = \varphi_{\max} . f_c \qquad (19)$$

where $\varphi_{i,min}$ is the value of the Priestley-Taylor parameter at the dry edge for a given value of $NDVI_i$, φ_{max} is the value of φ at the wet edge ($\varphi_{max} = (\Delta + \gamma)/\Delta$).

The fraction cover (f_c) is expressed as (Stisen *et al.*, 2008):

$$f_c = \left(\frac{NDVI - NDVI_{\min}}{NDVI_{\max} - NDVI_{\min}} \right)^2 \qquad (20)$$

where $NDVI_{min}$ and $NDVI_{max}$ are the minimum and maximum observed vegetation index values, corresponding respectively to bare soil and fully vegetated surfaces, defining the extremes of the trapezoid.

The third step is to interpolate φ between $\varphi_{i,min}$ and $\varphi_{i,max}$ within each *NDVI* class between the lowest temperature ($T_{s,i,min}$) at wet edge and highest temperature ($T_{s,i,max}$) at dry edge. The linear interpolation of φ_i with temperature leads to normalization of surface temperature and is given as:

$$\varphi_i = \frac{T_{0,i,\max} - T_{0,i}}{T_{0,i,\max} - T_{0,i,\min}} (\varphi_{\max} - \varphi_{i,\min}) + \varphi_{i,\min} \qquad (21)$$

where $T_{0,i,min}$ is the lowest surface temperature at the wet edge for a given NDVI and $T_{0,i,max}$ is the highest temperature at the dry edge for a given *NDVI*.

4. Results and discussion

Both SEBAL and T_s/VI trapezoid models are developed in C++ code. In the framework of this study, the modeling of the energy balance equation by SEBAL and T_s/VI trapezoid models allows us to show that the surface parameters, obtained from the satellite scanned spectral radiance in the optical and thermal infrared ranges, namely the albedo, the vegetation index and the surface temperature lead to determine the SEBAL-based latent heat flux (λE) as the residual term of the energy balance equation and the T_s/VI trapezoid-based λE directly by using the Priestley-Taylor equation. To evaluate the performance of the energy balance results from these two models, four statistical metrics were used: root mean square error (RMSE), mean absolute percent difference (MAPD), Bias and determination coefficient (R^2) (Timmermans *et al.*, 2007). Note that the validation of models outputs with an energy fluxes measurement system (such as the Bowen ratio system) is often used to assess the performance of energy balance models. However, this type of point-based comparison does not guarantee that the model provides consistent fluxes over the whole range of surface conditions that may exist in a landscape (Choi *et al.*, 2009; Khaldi *et al.*, 2011).

4.1 Surface temperature

The surface temperature (T_0) is indirectly related to the latent heat flux (λE) through the energy balance equation. It provides important information on surface moisture conditions that is useful to support agricultural water management at spatial scale. The analysis of the correlation between the satellite-derived surface temperature ($T_{0,Sat}$) and the ground-measured surface temperature ($T_{0,Ground}$), obtained by an Apogee infrared radiometer (IRTS-P), showed reliable results with R^2 of 0.93 (Fig. 6). However, $T_{0,Sat}$ in our case is slightly underestimated compared to the $T_{0,Ground}$ as evidenced by the RMSE of 3.11 °C (corresponding to MAPD of 10.47%) and a Bias of about −2 °C. The recorded temperature errors (3.6 to 18.5%) are relatively close to the values reported in previous studies with RMSE approximately ranging from 2.9 to 4.2 °C (Timmermans *et al.*, 2007; Santos *et al.*, 2020; Consoli and Vanella, 2014; Zou *et al.*, 2018). For example, a slightly similar RMSE and Bias (4.2 and −3.4 °C, respectively) were detected by Madugundu *et al.* (2017) in comparing $T_{0,Sat}$ against $T_{0,Ground}$ over an arid irrigated field in Saudi Arabia by using Landsat-8 data. In another study over the Texas High Plains, Chávez *et al.* (2009) reported remote sensing errors of 1.9 and 11.1% in estimating $T_{0,Sat}$ (compared to $T_{0,Ground}$) for sorghum and corn fields, respectively.

The analysis of the correlation between T_0 and λE for DOY 2 indicates significantly better agreement between these two variables, with R^2 of 0.93 and 0.97 for SEBAL and T_s/VI trapezoid, respectively (Fig. 7). Moreover, the NDVI and albedo parameters, even if they offer
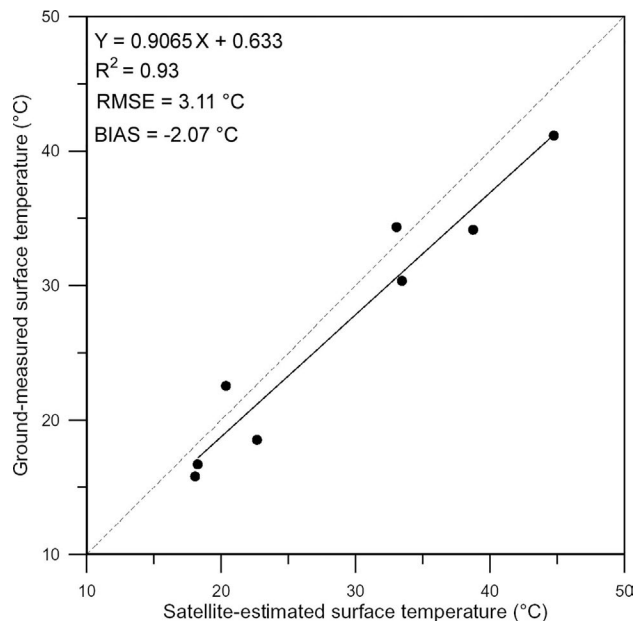

Figure 6 - Comparison between ground-measured and remote sensing-derived radiometrique surface temperature.
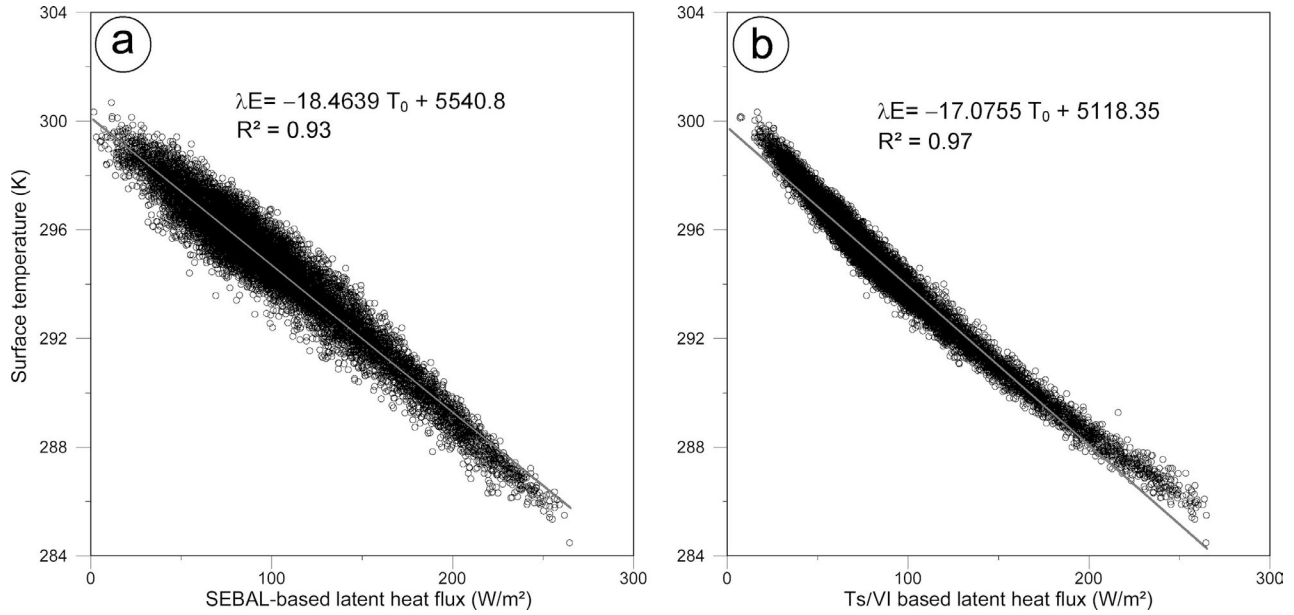
Figure 7 - Representation of the relationship between surface temperature and latent heat flux for the DOY 2: (a) SEBAL model and (b) Ts/VI trapezoid model.

interesting additional information in the interpretation of thermal infrared data (Carlson, 2007), are less significant in discriminating surface moisture conditions (Khaldi *et al.*, 2011).

Surface temperature variations in the study area are shown in Table 4. Higher values correspond to pixels where bare soils (dry pixels) are dominant, while low values are associated with irrigated dense vegetation (wet pixels). Similarly, the average surface temperature over dry pixels is higher than over wet pixels (Table 4).

4.2. Net Radiation

Higher values of net radiation (Rn) are recorded over dense vegetation cover ($NDVI > 0.7$) having optimum water supply conditions. Bare soils ($NDVI < 0.2$) are characterized by low Rn values, with an average of 235.2, 210.3, 388.3 and 444.8 W/m^2 for the DOY 271, 2, 75 and 130 respectively. The comparison between the ground-measured and satellite-estimated Rn values indicate better agreement, with RMSE of 28.7 W/m^2 (corresponding to MAPD of 14.6%), a Bias of 24.8 W/m^2 and R^2 of 0.92. The obtained RMSE and Bias values are relatively accu-

Table 4 - Instantaneous average values of parameters and surface energy fluxes above dry and wet pixels in the study area.

Parameter	Notation	Unit	28/09/2018 (DOY 271)		02/01/2019 (DOY 2)		16/03/2019 (DOY 75)		10/05/2019 (DOY 130)	
			Dry pixel	Wet Pixel	Dry pixel	Wet Pixel	Dry pixel	Wet Pixel	Dry pixel	Wet Pixel
NDVI	$NDVI$	–	0.08	0.77	0.11	0.73	0.08	0.79	0.08	0.70
Albedo	r_0	–	0.33	0.19	0.27	0.18	0.25	0.21	0.30	0.18
Emissivity	ε_0	–	0.91	0.99	0.92	0.99	0.91	0.99	0.91	0.99
Surface temperature	T_0	K	312.6	295.1	299.7	284.8	303.5	289.7	327.3	300.3
Net radiation	Rn	W/m^2	161.1	323.2	163.3	274.0	361.3	429.6	370.4	645.0
Soil heat flux	G	W/m^2	33.3	20.3	21.2	9.8	51.9	20.8	101.3	57.8
Friction velocity	u^*	s/m	0.31	0.39	0.26	0.29	0.34	0.40	0.27	0.28
Monin-Oubukhov length	L	m	−22.2	−814.5	−11.2	−765.5	−11.1	−440.4	−6.80	−101.3
Aerodynamic resistance to heat transport	r_{ah}	s/m	19.6	18.4	21.3	24.6	16.3	19.2	18.7	26.5
Sensible heat flux	H	W/m^2	137.3	0.4	142.1	0.7	309.4	0.2	269.1	0.8
Latent heat flux (SEBAL)	λE	W/m^2	0	302.6	0	263.2	0	426.3	0	587.2
Latent heat flux (T$_s$/VI trapezoid)	λE	W/m^2	0	303.0	0	264.1	0	408.3	0	582. 3
Near-surface air temperature difference	dT	°C	2.34	0	2.61	0	3.68	0	4.54	0

rate compared to those reported by the earlier studies of Santos *et al.* (2020), where RMSE and Bias values were respectively of 32.2 and 27.3 W/m^2, Choi *et al.* (2009), where the RMSE ranged from 20 to 30 W/m^2 and Bias was about 20 W/m^2, Tang and Li, (2015), where the RMSE was 30.7 W/m^2 and Bias was 11.3 W/m^2, and Zou *et al.* (2018) where RMSE and Bias were 66.9 and 45.6 W/m^2, respectively.

4.3. Soil heat flux

For the image acquired on autumn (DOY 271), the average soil heat flux (*G*) is 37.7 W/m^2. However, the average of *G* is higher (102.2 W/m^2) in early summer (DOY 130), when the temperature is high. Bare soils offer the highest values of *G*, about 38.6, 21.2, 48.3 and 104.4 W/m^2 for the DOY 271, 2, 75 and 130, respectively. For surfaces fully covered by vegetation (*NDVI* > 0.7), the soil heat flux is of 23.8, 10.8, 25.8 and 59.5 W/m^2 for the DOY 271, 2, 75 and 130, respectively.

Comparison between the ground-measured and satellite-estimated soil heat flux values indicates that the model leads to an underestimation of the *G* flux with RMSE of 15.2 W/m^2 (corresponding to MAPD of 29.2%). This result is quite similar to that obtained on the Ksar Chellala plain in Algeria by Hamimed *et al.*(2014), where RMSE was 13.2 W/m^2 (MAPD~45%), on the Ghriss plain in Algeria by Nehal *et al.* (2017), where RMSE was 14 W/m^2 (MAPD~27%), over an alfalfa field in Eastern Colorado by Mkhwanazi and Chavez, (2012), with RMSE of 14.2 W/m^2 (MAPD~27%), and on the Low-Middle São Francisco River basin by Teixeira *et al.* (2009) where the local calibration yielded a R^2 of 0.81 and RMSE of 13.3 W/m^2. The underestimation of *G* can be explained by the uncertainty of the intermediate variables used in the model (such as albedo, *NDVI* and surface temperature). Despite this imprecision, *G* flux values are lower than the other energy fluxes and consequently has a small impact on the available energy (*Rn-G*) (Nehal *et al.*, 2017).

4.4. Sensible heat flux

In the studies of ET estimation through the energy balance equation, the sensible heat flux evaluation is the most delicate for residual models such as SEBAL (Hamimed *et al.*, 2014). To reduce errors due to this flux, SEBAL used an approach based on the Monin-Oubukhov similarity theory in the atmospheric boundary layer. In fact, the surface boundary layer modeling allows mapping the sensible heat flux which is obtained by estimating two key parameters of the energy balance regulation, depending on the surface type and its thermodynamic properties which are the aerodynamic resistance to heat transfer (r_{ah}) and the surface-air temperatures difference.

In the sensible heat flux (*H*) estimation, wet pixels are identified on dense vegetation cover (*NDVI* > 0.7), with an average temperature values of 295.1, 284.8, 289.7

and 300.3 K for the DOY 271, 2, 75, 130 respectively (Table 4).

We note also on Table 4 that for dry pixels (bare soil and urban) the aerodynamic resistance to heat transfer (r_{ah}) is low (19.6, 21.3, 16.3 and 18.7 s/m for the DOY 271, 2, 75, 130, respectively), causing the release of sensible heat to the atmosphere. This is justified by high differences between surface and air temperatures. However, for wet pixels (freshly irrigated plots) r_{ah} values are high (18.4, 24.6, 19.2 and 26.5 s/m for the DOY 271, 2, 75, 130, respectively) because the available energy (*Rn - G*) is mainly consumed by ET. This differentiation of the sensible heat flux for dry and wet pixels is caused by the surface water status and its influence on the energy partition between the latent and sensible heat. Specifically, wet surfaces are individualized by low *H* values while high *H* values are assigned to dry areas (Table 4). Compared to field BREB observations, SEBAL-estimated sensible heat flux (*H*) agrees relatively well, yielding a RMSE and Bias values of 55.4 and 21.6 W/m^2, respectively. These results indicate that SEBAL slightly overestimated *H* flux by a relative Bias of around 17%. Therefore, they still considered in reasonable agreement with the Bowen ratio measurements, having ~20% uncertainty (Kustas and Norman, 1999; Liu and Xu, 2019; Timmermans *et al.*, 2007), and are in good agreement with the values reported by the previous studies of Tang and Li, (2015), Santos *et al.* (2020), Wagle *et al.* (2017) and Ochege *et al.* (2019), indicating RMSE values of 46.4, 82.8, 72 and 48.29 W/m^2, respectively. However, the T$_s$/VI trapezoid model exhibited that it has significantly greater difficulty in estimating *H* flux (deduced as *H = Rn - G - λ*E), producing a RMSE of 97.3 W/m^2 and Bias of 78.5 W/m^2, which indicates an overestimation of *H* by a relative Bias of about 37%. The errors on T$_s$/VI trapezoid model estimates are slightly similar to those detected by Tang and Li (2015), with RMSE and Bias values were 119 and 98 W/m^2, respectively. This indicates that the T$_s$/VI trapezoid model is more sensitive to the estimated available energy (*Rn-G*) than SEBAL, and is because SEBAL is designed to compensate for the available energy and *H*-flux Bias, by using a contextual image-based calibration approach (Bastiaanssen *et al.*, 1998).

4.5. Latent heat flux

In the irrigation scheme, computed water allocations can be updated using the information obtained by some irrigation performance indicators, such as uniformity and adequacy (Bastiaanssen *et al.*, 1996). The latent heat flux (*λE*, corresponding to the energy consumed by ET) can be used to express the uniformity of crop water use, which is related to the equity of irrigation water distribution, or to detect the adequacy of regional water management, through the evaporative fraction (*EF*) which is mainly deduced from *λE* (Eq. (18)).

The latent heat flux is generally high for dense canopy and low for dry bare soils having high surface temperatures, low net radiations and high sensible heat fluxes. Table 5 summarizes the results of energy fluxes and moisture indicators obtained from the two models (SEBAL and T$_s$/VI trapezoid) for different land use categories. It shows that high values of ET (λE) are observed over the irrigated areas with dense vegetation, while low values are over the bare soils, corresponding to high values of albedo. This allows emphasizing that the spatial distribution of SEBAL and T$_s$/VI trapezoid-derived ET is relatively well correlated to the water regimes of the different land use units.

Overall, both SEBAL and T$_s$/VI trapezoid models reproduce the estimated latent heat fluxes fairly well, compared to field BREB observations. The SEBAL-estimated latent heat flux values shows a slight discrepancy and better performance than T$_s$/VI trapezoid, with RMSE of 49.1 W/m^2 (corresponding to MAPD of 18.2%), a Bias of −15.1 W/m^2 (relative Bias = −5.8%) and R^2 of 0.77 (Fig. 8a). These statistics are in good agreement with those obtained on Caatinga biome site (RMSE = 82.8 W/m^2 and Bias = −18 W/m^2) by Santos *et al.* (2020), on the SMA-CEX site (RMSE = 57 W/m^2 and Bias = −29 W/m^2) by Choi *et al.* (2009), and on sub-humid grassland (Southern Great Plains '97) and semi-arid rangeland (Monsoon '90) (RMSE = 49 W/m^2 and Bias = −13 W/m^2) by Timmer-

mans *et al.* (2007). However, the T$_s$/VI trapezoid model tends to significantly underestimate latent heat flux with a Bias of −39.2 W/m^2 (corresponding to −15% in relative value), RMSE of 52.5 W/m^2 (MAPD=20.7%) and a determination coefficient (R^2) of 0.81 (Fig. 8b). This significant underestimation of T$_s$/VI trapezoid-derived λE flux was also demonstrated by Choi *et al.* (2009), Tang and Li (2015) and Lian and Huang (2016).

Figure 9 shows the spatial distributions of the latent heat fluxes (λE) derived from the two models. Although the same anchor pixels (hot and cold) were selected with the two models, it was observed that the SEBAL model predicted a slightly higher λE than the T$_s$/VI trapezoid model (Fig. 10), especially for DOY 130 (10 May 2019), as shown in Fig.10d. These spatial patterns are likely due to different approaches used to estimate H and λE by the two models. The SEBAL calculates H using a single-source temperature gradient technique for heat transport, accounting for stability effects based on the Monin-Obukhov theory, and λE is computed as a residual of the energy balance equation, while the T$_s$/VI trapezoid model calculates λE directly from Eq. (10), but H is calculated as a residual of the energy balance equation. Based on the identified spatial patterns for H and λE, the SEBAL computational scheme seems to be more physically comprehensive considering the stability for the aerodynamic resistance of heat transport (Wagle *et al.*, 2017).

Table 5 - Variation of surface energy fluxes and moisture indicators with land use over the Habra plain.

| Satellite image date	Type of land use	Rn	G	SEBAL			T$_s$/VI trapezoid		
				H	λE	EF	φ	λE	EF
	Bare soil	235.25	38.47	107.05	95.13	0.47	0.38	54.85	0.27
	Sparse vegetation	299.54	34.63	49.48	217.88	0.818	0.98	186.56	0.69
	Moderate Vegetation	312.43	31.33	35.819	247.08	0.87	1.16	232.21	0.82
	Dense Vegetation	316.26	27.91	28.29	261.49	0.90	1.26	259.27	0.89
28/09/2018 (DOY 271)	Very dense Vegetation	312.73	23.78	23.00	267.12	0.92	1.35	277.74	0.96
	Bare soil	210.33	20.75	93.65	95.92	0.49	0.06	82.06	0.42
	Sparse vegetation	250.57	17.32	44.38	188.86	0.80	0.47	174.18	0.74
	Moderate Vegetation	258.81	15.40	31.81	211.59	0.867	0.81	206.43	0.84
	Dense Vegetation	262.73	13.63	24.39	224.71	0.90	1.14	227.87	0.91
02/01/2019 (DOY 2)	Very dense Vegetation	260.38	11.58	20.53	228.27	0.92	1.50	241.49	0.97
	Bare soil	388.26	50.69	273.45	64.12	0.19	0.24	53.23	0.16
	Sparse vegetation	398.51	47.83	212.71	137.96	0.39	0.49	115.68	0.33
	Moderate Vegetation	413.37	44.10	155.97	213.30	0.57	0.76	187.06	0.50
	Dense Vegetation	430.78	38.80	105.86	286.12	0.73	1.04	272.90	0.69
16/03/2019 (DOY 75)	Very dense Vegetation	438.51	28.97	58.07	351.47	0.86	1.36	370.22	0.90
	Bare soil	444.87	105.99	227.32	111.55	0.32	0.23	56.45	0.16
	Sparse vegetation	476.64	103.68	177.91	195.05	0.51	0.41	111.02	0.29
	Moderate Vegetation	531.24	98.86	120.56	311.81	0.72	0.65	205.02	0.47
	Dense Vegetation	574.22	88.16	69.47	416.59	0.85	0.94	331.49	0.68
10/05/2019 (DOY 130)	Very dense Vegetation	600.65	71.84	28.86	499.94	0.94	1.23	468.94	0.88
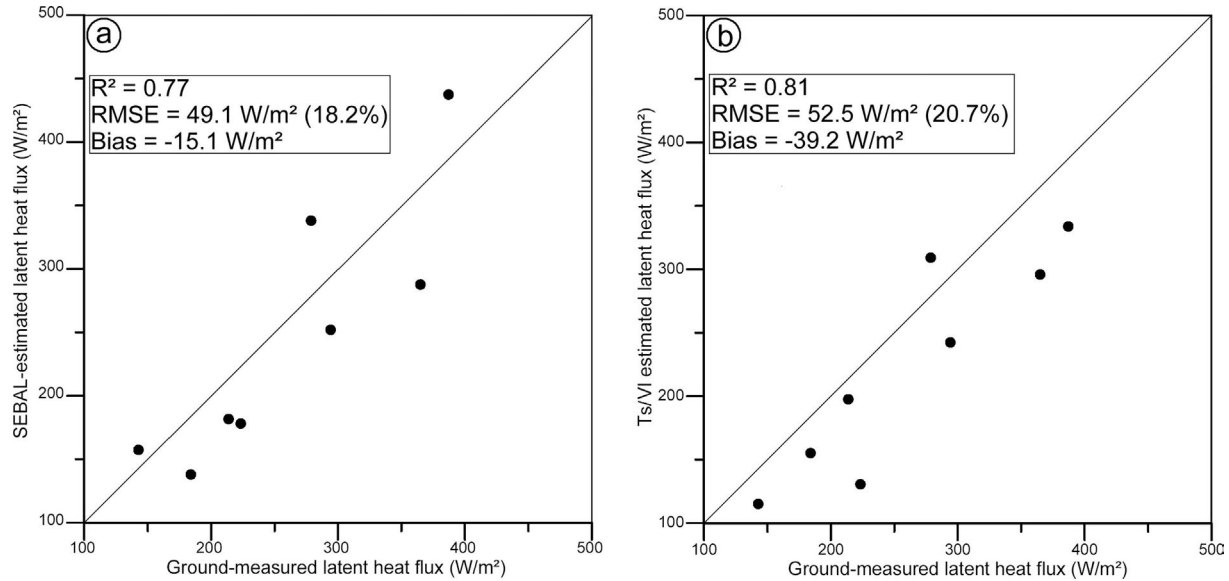
Figure 8 - Comparison between the ground-based and satellite-derived estimates of latent heat fluxes: (a) SEBAL model versus ground observations and (b) Ts/VI trapezoid model versus ground observations.
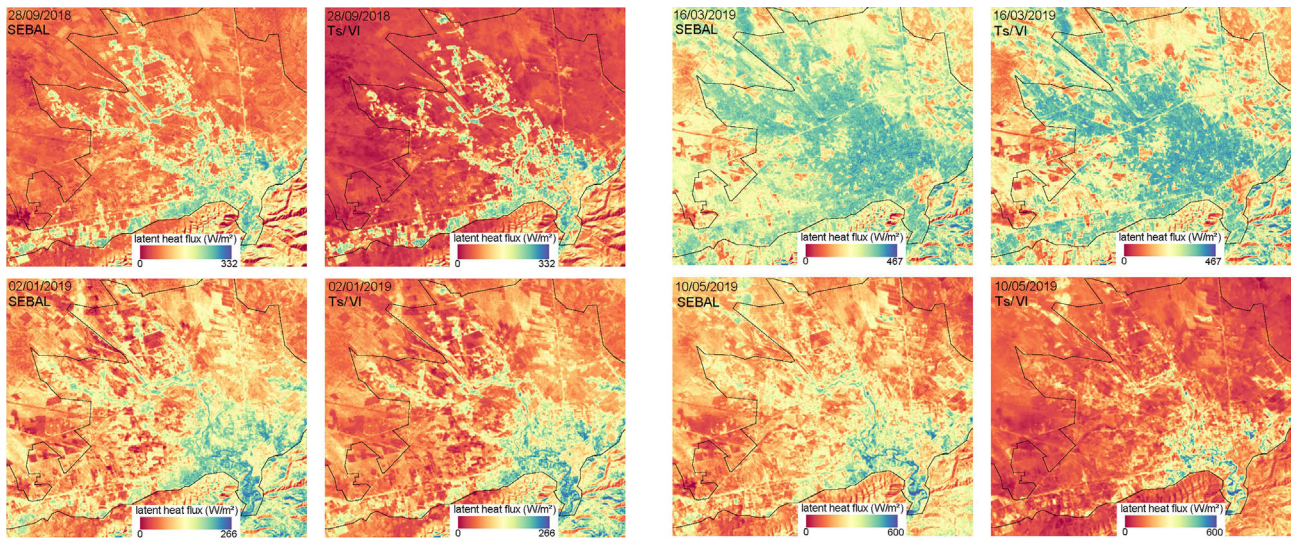

Figure 9 - Spatial distributions of the latent heat fluxes estimated with SEBAL and Ts/VI trapezoid on 28 September 2018, 2 January 2019, 16 March 2019 and 10 May 2019.

The comparison of the latent heat flux estimates with SEBAL and T_s/VI trapezoid models is shown in Fig.10. In general, a good agreement with determination coefficients (R^2) of 0.95, 0.95, 0.96 and 0.91 is shown for the DOY 271, 2, 75 and 130 respectively, with RMSE of 33.6, 14.1, 25.9 and 56.3 W/m^2, respectively (Fig.10). The result of this comparison leads to the conclusion that the two models provide close outputs and suggests that both models can be considered as operational approaches for monitoring ET and surface water status over agricultural areas having limited amount of ground information. We can also note that the simple contextual methods, such as T_s/VI tra-

pezoid model, have the potential to provide ET estimations consistent with the rather complex physically-based SEBAL model, as indicated by Lian and Huang (2016). However, ET estimations from the T_s/VI trapezoid model are quite sensitive to derived (Rn-G), T_0 and EF, while SEBAL can compensate for errors in estimated (Rn-G) and T_0 by using a hot and cold pixel based contextual approach to internally calibrate sensible heat flux through an iterative approach.

Different moisture indicators, such as evaporative fraction (EF) and surface resistance to evaporation (r_s), that can provide direct information on the stress condition
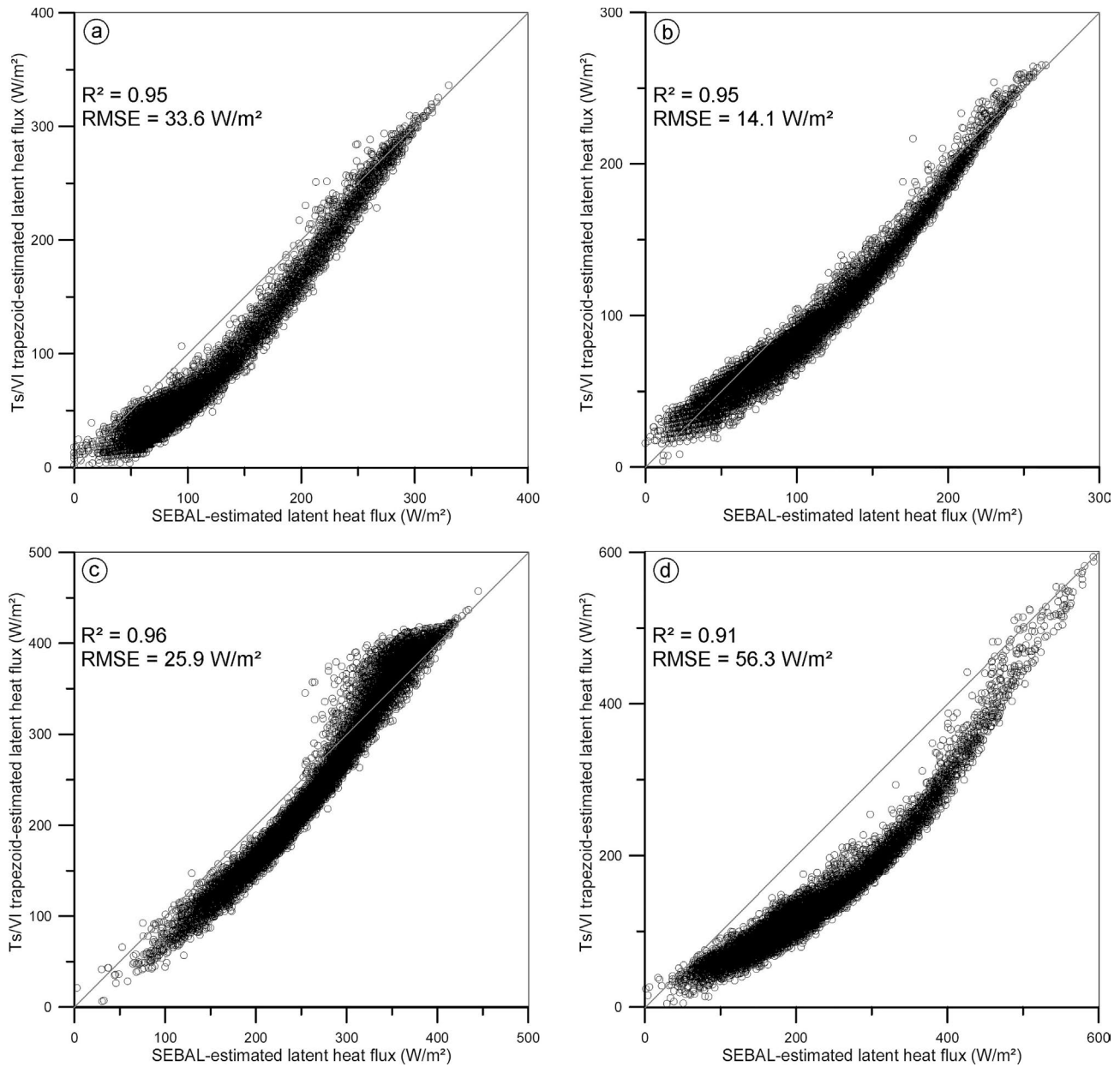
Figure 10 - Comparison of the latent heat flux estimates with SEBAL and Ts-VI trapezoid on (a) 28 September 2018, (b) 2 January 2019, (c) 16 March 2019 and (d) 10 May 2019 over the Habra plain.

of crops, are computed from the latent heat flux (λE). In Figs. 11 and 12, we represent and compare the spatial distributions of the evaporative fraction obtained by SEBAL and T_s/VI trapezoid model for the DOY 2. This comparison shows good agreement, with R^2 of 0.92 and RMSE of 0.074 (-), and justifies that both models produce nearly the same output.

Another way to validate our results is to analyze the frequency distribution of the surface resistance to evaporation (Fig. 13). Bastiaanssen *et al.* (1996) showed that for most crops covering fully soil (*NDVI* > 0.65), this resistance vary between 10 and 300 s/m with generally
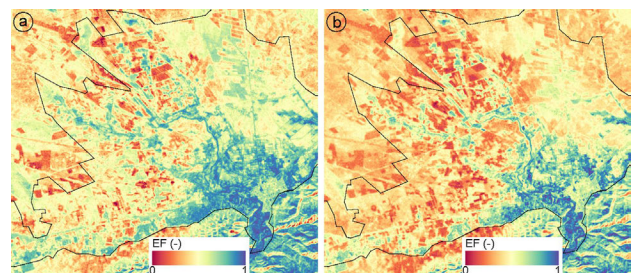

Figure 11 - Comparison of the evapotarive fraction: (a) SEBAL, (b) Ts/VI trapezoid on 2 January 2019 (DOY 2).
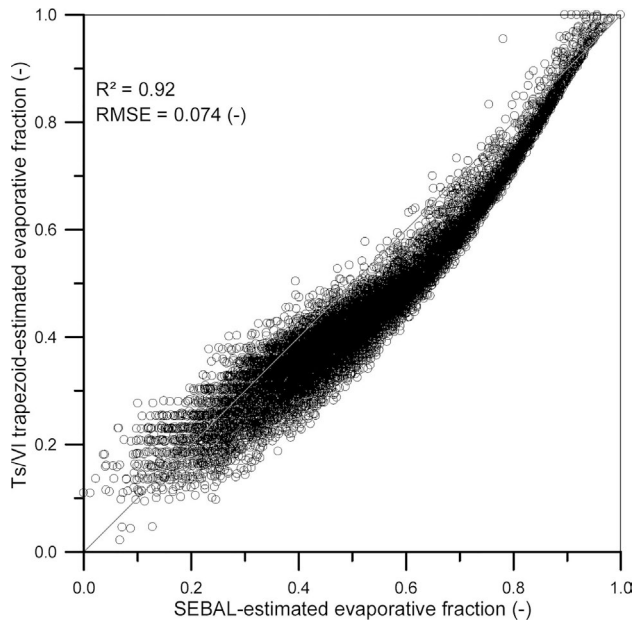
Figure 12 - Density plot of SEBAL versus Ts/VI trapezoid evaporative fraction on 2 January 2019 (DOY 2).

peaking in the class of 30 to 80 s/m. There is a general consensus that the surface resistance for crops which cover the soil entirely lies in approximately the same range (Chávez and López-Urrea, 2019, Bougeault *et al.*, 1991). The results shown in Fig. 13 are approximately consistent with this indication.

5. Conclusion

Different models have been developed to estimate ET from remote sensing data. In this paper, SEBAL and T_s/VI trapezoid models were applied using Landsat-8 OLI/TIRS data over the Habra plain (western Algeria), a semiarid region with heterogeneous surface conditions, to estimate actual ET. The models outputs were compared with field observations using BREB method, to identify the most appropriate model.

A significant discrepancy between remote sensing and ground estimates of latent heat flux is shown, with RMSE value of 49.1W/m^2 and 52.5 W/m^2 for SEBAL and T_s/VI trapezoid respectively. That means 18.2% and 20.7% in relative terms and a determination coefficient
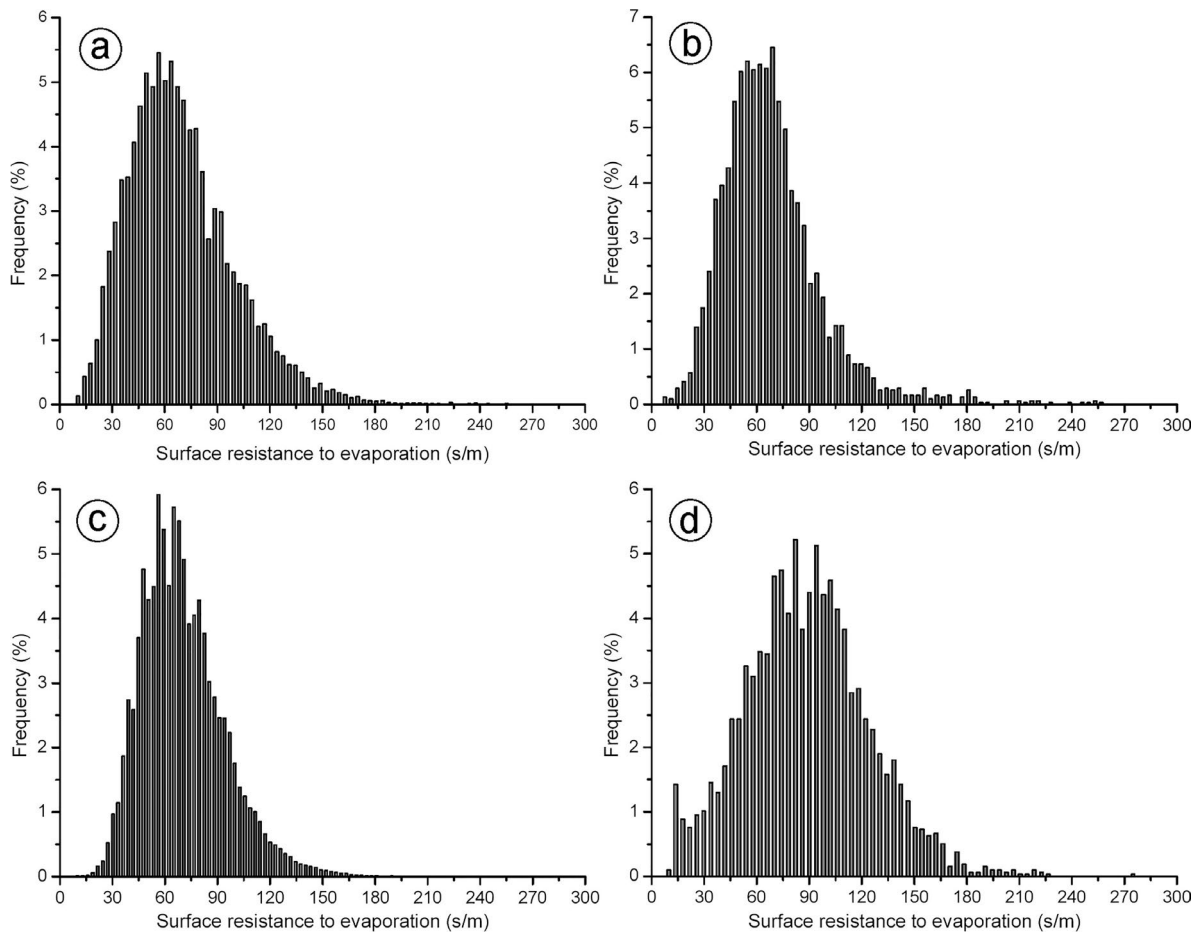

Figure 13 - Frequency distributions of the surface resistance to evaporation estimated with SEBAL on 28 September 2018 (a), 2 January 2019 (b), 16 March 2019 (c) and 10 May 2019 (d) for pixels with NDVI values more than 0.65.

(R^2) of 0.77 and 0.81 respectively. These results are ascribed to errors committed in estimating the net radiation, soil heat flux and the sensible heat flux. These differences can be explained by the inaccuracies on the intermediate variables such as surface emissivity, soil heat flux, roughness length and air temperature and by excess in the net radiation occurred in the irrigated plots of this semi-arid region, due to the advection effects.

     The results presented above confirm the possibilities offered by the Landsat-8 OLI/TIRS satellite data to solve the energy balance equation and to be routinely applied as a tool for providing both historical and near-real time ET for performing a better management of the agricultural water resources of the area. Despite the recorded inaccuracies, the obtained results show that both SEBAL and T$_s$/VI trapezoid models provide close outputs and suggest that these models are suitable approaches to monitor actual ET and surface water status over agricultural areas where ground information is scarce or difficult to collect.

Acknowledgment

References

ALLEN, R.G.; PEREIRA, L.S.; RAES, D.; SMITH., M. **Crop Evapotranspiration: Guidelines for Computing Crop Water Requirements**. Irrigation and Drainage Paper 56. Rome: Food and Agriculture Organization of the United Nations (FAO), p. 300, 1998.

ALLEN, R.G.; TASUMI, M.; TREZZA, R. Satellite-based energy balance for mapping evapotranspiration with internalized calibration (METRIC) - Model. **Journal of Irrigation and Drainage Engineering**, v. 133, n. 4, p. 380-394, 2007.

ALLIES, A.; DEMARTY, J.; OLIOSO, A.; MOUSSA, I.B.; ISSOUFOU, H.B.A.; VELLUET, C.; BAHIR, M.; MAÏN-ASSARA, I.; OÏ, M.; CHAZARIN, J.P.; CAPPELAERE, B. Evapotranspiration estimation in the Sahel using a new ensemble-contextual method. **Remote Sensing**, v. 12, n. 3, p. 380, 2020.

ANDERSON, M.C.; NORMAN, J.M.; MECIKALSKI, J.R.; OTKIN, J.A.; KUSTAS, W.P. A climatological study of evapotranspiration and moisture stress across the continental United States based on thermal remote sensing: 1. Model formulation. **Journal of Geophysical Research**, v. 112, D10117, p. 1-13, 2007.

BAI, L.; LONG, D.; YAN, L. Estimation of surface soil moisture with downscaled land surface temperatures using a data fusion approach for heterogeneous agricultural land. **Water Resources Research**, v. 55, n. 2, p. 1105-1128, 2019.

BASTIAANSSEN, W.G. SEBAL-based sensible and latent heat fluxes in the irrigated Gediz Basin, Turkey. **Journal of Hydrology**, v. 229, n. 1-2, p. 87-100, 2000.

BASTIAANSSEN, W.G.; MENENTI, M.; FEDDES, R.A.; HOLTSLAG, A.A.M. A remote sensing surface energy balance algorithm for land (SEBAL). 1. Formulation. **Journal of Hydrology**, v. 212, p. 198-212, 1998.

BASTIAANSSEN, W.G.; VAN DER WAL, T.; VISSER, T.N.M. Diagnosis of regional evaporation by remote sensing to support irrigation performance assessment. **Irrigation and Drainage Systems**, v. 10, n. 1, p. 1-23. 1996.

BASTIAANSSEN, W.G.M.; NOORDMAN, E.J.M.; PELGRUM, H.; DAVIDS, G.; THORESON, B.P.; ALLEN, R.G. SEBAL model with remotely sensed data to improve water-resources management under actual field conditions. **Journal of Irrigation and Drainage Engineering**, v. 131, n. 1, p. 85-93, 2005.

BENZATER, B.; ELOUISSI, A.; BENARICHA, B.; HABI, M. Spatio-temporal trends in daily maximum rainfall in northwestern Algeria (Macta watershed case, Algeria). **Arabian Journal of Geosciences**, v. 12, n. 11, p. 370, 2019.

BENZATER, B.; ELOUISSI, A.; DABANLI, I.; BENARICHA, B.; HAMIMED, A. Extreme rain trend analysis in Macta watershed North West Algeria. **Arabian Journal of Geosciences**, v. 14, n. 4, p. 1-14, 2021.

BIGEARD, G.; COUDERT, B.; CHIROUZE, J.; ER-RAKI, S.; BOULET, G.; CESCHIA, E.; JARLAN, L. Ability of a soil-vegetation-atmosphere transfer model and a two-source energy balance model to predict evapotranspiration for several crops and climate conditions. **Hydrology and Earth System Sciences**, v. 23, n. 12, p. 5033-5058, 2019.

BOEGH, E.; SOEGAARD, H.; THOMSEN, A. Evaluating evapotranspiration rates and surface conditions using Landsat TM to estimate atmospheric resistance and surface resistance. **Remote Sensing of Environment**, v. 79, n. 2-3, p. 329-343, 2002.

BOUGEAULT, P.; NOILHAN, J.; LACARRERE, P.; MASCART, P. An experiment with an advanced surface parameterization in a mesobeta-scale model. Part I: Implementation. **Monthly Weather Review**, v. 119, n. 10, p. 2358-2373, 1991.

BOULET, G.; DELOGU, E.; SAADI, S.; CHEBBI, W.; OLIOSO, A.; MOUGENOT, B.; PASCAL FANISE, P.; LILI-CHABAANE, Z.; LAGOUARDE, J.P. Evapotranspiration and evaporation/transpiration partitioning with dual source energy balance models in agricultural lands. **Proceedings of the International Association of Hydrological Sciences**, v. 380, p. 17-22, 2018.

BOULET, G.; JARLAN, L.; OLIOSO, A.; NIETO, H. Evapotranspiration in the Mediterranean region. In: **Water Resources in the Mediterranean Region**. ZRIBI, M.; BROCCA, L.; TRAMBLAY, Y.; MOLLE, F. (eds.). Amsterdam: Elsevier, p. 23-49, 2020.

BRUTSAERT, W. **Evaporation Into the Atmosphere: Theory, History and Applications**. Dordrecht: Springer, p. 299, 2013.

CARLSON, T. An overview of the "triangle method" for estimating surface evapotranspiration and soil moisture from satellite imagery. **Sensors**, v. 7, n. 8, p. 1612-1629, 2007.

CARLSON, T.N.; PETROPOULOS, G.P. A new method for estimating of evapotranspiration and surface soil moisture from optical and thermal infrared measurements: the sim-

plified triangle. **International Journal of Remote Sensing**, v. 40, n. 20, p. 7716-7729, 2019.

CHÁVEZ, J.L.; GOWDA, P.H.; HOWELL, T.A.; COPELAND, K.S. Radiometric surface temperature calibration effects on satellite based evapotranspiration estimation. **International Journal of Remote Sensing**, v. 30, n. 9, p. 2337-2354, 2009.

CHÁVEZ, J.L.; LÓPEZ-URREA, R. One-step approach for estimating maize actual water use: Part I. Modeling a variable surface resistance. **Irrigation Science**, v. 37, n. 2, p. 123-137, 2019.

CHEBBI, W.; BOULET, G.; LE DANTEC, V.; LILI-CHA-BAANE, Z.; FANISE, P.; MOUGENOT, B.; AYARI, H. Analysis of evapotranspiration components of a rainfed olive orchard during three contrasting years in a semi-arid climate. **Agricultural and Forest Meteorology**, v. 256, p. 159-178, 2018.

CHEN, J.M.; LIU, J. Evolution of evapotranspiration models using thermal and shortwave remote sensing data. **Remote Sensing of Environment**, v. 237, n. 111594, p. 20, 2020.

CHEN, X.; SU, Z.; MA, Y.; MIDDLETON, E.M. Optimization of a remote sensing energy balance method over different canopy applied at global scale. **Agricultural and Forest Meteorology**, v. 279, n. 107633, 2019.

CHOI, M.; KUSTAS, W.P.; ANDERSON, M.C.; ALLEN, R.G.; LI, F.; KJAERSGAARD, J.H. An intercomparison of three remote sensing-based surface energy balance algorithms over a corn and soybean production region (Iowa, US) during SMACEX. **Agricultural and Forest Meteorology**, v. 149, n. 12, p. 2082-2097, 2009.

CONSOLI, S.; VANELLA, D. Comparisons of satellite-based models for estimating evapotranspiration fluxes. **Journal of Hydrology**, v. 513, p. 475-489, 2014.

ELOUISSI, A.; HABI, M.; BENARICHA, B.; BOUALEM, S.A. Climate change impact on rainfall spatio-temporal variability (Macta watershed case, Algeria). **Arabian Journal of Geosciences**, v. 10, n. 22, p. 496, 2017.

GAVILÁN, S.A.; PASTORE, J.I.; QUIGNARD, I.; MARASCO, N.D.; ACEÑOLAZA, P.G. Energy balance model as real evapotranspiration estimator with satellite and meteorological data. **Interciencia**, v. 44, n. 7, p. 400-407, 2019.

HAMIMED, A.; NEHAL, L.; KHALDI, A.; AZZAZ, H. Contribution à la spatialisation de l'évapotranspiration d'un agro-système semi-aride en Algérie par utilisation de la télédétection et du modèle METRIC. **Physio-Géo. Géographie Physique et Environnement**, v. 8, p. 197-213, 2014.

HU, X.; SHI, L.; LIN, L.; ZHA, Y. Nonlinear boundaries of land surface temperature-vegetation index space to estimate water deficit index and evaporation fraction. **Agricultural and Forest Meteorology**, v. 279, p. 107736, 2019.

HUANG, L.; CAI, J.; ZHANG, B.; CHEN, H.; BAI, L.; WEI, Z.; PENG, Z. Estimation of evapotranspiration using the crop canopy temperature at field to regional scales in large irrigation district. **Agricultural and Forest Meteorology**, v. 269, p. 305-322, 2019.

JIANG, L.; ISLAM, S. Estimation of surface evaporation map over southern Great Plains using remote sensing data. **Water Resources Research**, v. 37, n. 2, p. 329-340, 2001.

KHALDI, A.; HAMIMED, A.; MEDERBAL, K.; SEDDINI, A. Obtaining evapotranspiration and surface energy fluxes with remotely sensed data to improve agricultural water management. **African Journal of Food, Agriculture, Nutrition and Development**, v. 11, p. 1, 2011.

KHALDI, A.; KHALDI, A.; HAMIMED, A. Using the Priestley-Taylor expression for estimating actual evapotranspiration from satellite Landsat ETM+ data. **Proceedings of the International Association of Hydrological Sciences**, v. 364, p. 398-403, 2014.

KUSTAS, W.P.; NORMAN, J.M. Evaluation of soil and vegetation heat flux predictions using a simple two-source model with radiometric temperatures for partial canopy cover. **Agricultural and Forest Meteorology**, v. 94, n. 1, p. 13-29, 1999.

KUSTAS, W.P.; ALFIERI, J.G.; NIETO, H.; WILSON, T.G.; GAO, F.; ANDERSON, M.C. Utility of the two-source energy balance (TSEB) model in vine and interrow flux partitioning over the growing season. **Irrigation Science**, v. 37, n. 3, p. 375-388, 2019.

KUSTAS, W.P.; CHOUDHURY, B.J.; MORAN, M.S.; REGINATO, R.J.; JACKSON, R.D.; GAY, L.W.; WEAVER, H.L. Determination of sensible heat flux over sparse canopy using thermal infrared data. **Agricultural and Forest Meteorology**, v. 44, n. 3-4, p. 197-216, 1989.

LIAN, J.; HUANG, M. Comparison of three remote sensing based models to estimate evapotranspiration in an oasis-desert region. **Agricultural Water Management**, v. 165, p. 153-162, 2016.

LIU, S.; XU, Z. Micrometeorological methods to determine evapotranspiration. In: **Observation and Measurement of Ecohydrological Processes**, LI, X.; VEREECKEN, H. (eds.). Berlin Heidelberg: Springer, p. 201-240, 2019.

MADUGUNDU, R.; AL-GAADI, K.A.; TOLA, E.; HASSABALLA, A.A.; PATIL, V.C. Performance of the METRIC model in estimating evapotranspiration fluxes over an irrigated field in Saudi Arabia using Landsat-8 images. **Hydrology and Earth System Sciences**, v. 21, n. 12, p. 6135, 2017.

MKHWANAZI, M.M.; CHAVEZ, J.L. Using METRIC to estimate surface energy fluxes over an alfalfa field in Eastern Colorado. **Hydrology Days**, p. 90-98, 2012, available at: http://hydrologydays.colostate.edu/Papers_2012/Mcebisi_paper.pdf, access: 5 July 2019.

MORAN, M.S.; CLARKE, T.R.; INOUE, Y.; VIDAL, A. Estimating crop water deficit using the relation between surface-air temperature and spectral vegetation index. **Remote Sensing of Environment**, v. 49, n. 3, p. 246-263, 1994.

NEHAL, N.; HAMIMED, A.; KHALDI, A.; SOUIDI, Z.; ZAAGANE, M. evapotranspiration and surface energy fluxes estimation using the Landsat-7 Enhanced Thematic Mapper Plus image over a semiarid agrosystem in the north-west of Algeria. **Revista Brasileira de Meteorologia**, v. 32, n. 4, p. 691-702, 2017.

OCHEGE, F.U.; LUO, G.; OBETA, M.C.; OWUSU, G.; DUULATOV, E.; CAO, L.; NSENGIYUMVA, J.B. Mapping evapotranspiration variability over a complex oasis-desert ecosystem based on automated calibration of Landsat 7

ETM+ data in SEBAL. **GIScience & Remote Sensing**, v. 56, n. 8, p. 1305-1332, 2019.

OLIOSO, A.; INOUE, Y.; ORTEGA-FARIAS, S.; DEMARTY, J.; WIGNERON, J.P.; BRAUD, I.; JACOB, F. LECHAR-PENTIER, P.; OTTLE, C.; CALVET, J.C.; BRISSON, N. Future directions for advanced evapotranspiration modeling: Assimilation of remote sensing data into crop simulation models and SVAT models. **Irrigation and Drainage Systems**, v. 19, n. 3-4, p. 377-412, 2005.

QUALLS, R.J.; BRUTSAERT, W. Effect of vegetation density on the parameterization of scalar roughness to estimate spatially distributed sensible heat fluxes. **Water Resources Research**, v. 32, n. 3, p. 645-652, 1996.

RAMÍREZ-CUESTA, J.M.; ALLEN, R.G.; INTRIGLIOLO, D.S.; KILIC, A.; ROBISON, C.W.; TREZZA, R.; SAN-TOS, C.; LORITE, I.J. METRIC-GIS: An advanced energy balance model for computing crop evapotranspiration in a GIS environment. **Environmental Modelling & Software**, v. 131, n. 104770, 2020.

ROERINK, G.J.; SU, Z.; MENENTI, M. S-SEBI: A simple remote sensing algorithm to estimate the surface energy balance. **Physics and Chemistry of the Earth**, v. 25, n. 2, p. 147-157, 2000.

SANDHOLT, I.; RASMUSSEN, K.; ANDERSEN, J. A simple interpretation of the surface temperature/vegetation index space for assessment of surface moisture status. **Remote Sensing of Environment**, v. 79, n. 2-3, p. 213-224, 2002.

SANTOS, C.A.C.; MARIANO, D.A.; NASCIMENTO, F.C.A.; DANTAS, F.R.C.; OLIVEIRA, G.; SILVA, M.T.; SILVA, L.L.; SILVA, B.B.; BEZERRA, B.G.; SAFA, B.; MEDEI-ROS, S.S.; NEALE, C.M.U. Spatio-temporal patterns of energy exchange and evapotranspiration during an intense drought for drylands in Brazil. **International Journal of Applied Earth Observation and Geoinformation**, v. 85, n. 101982, 2020.

STISEN, S.; SANDHOLT, I.; NØRGAARD, A.; FENSHOLT, R.; JENSEN, K.H. Combining the triangle method with thermal inertia to estimate regional evapotranspiration-Applied to MSG-SEVIRI data in the Senegal River basin. **Remote Sensing of Environment**, v. 112, n. 3, p. 1242-1255, 2008.

SU, Z. The Surface Energy Balance System (SEBS) for estimation of turbulent heat fluxes. **Hydrology and Earth System Sciences**, v. 6, n. 1, p. 85-100, 2002.

SUTTON, K.; ZAIMECHE, S. Water resource problems in Algeria. **Méditerranée**, v. 76, n. 3, p. 35-43, 1992.

TANG, R.; LI, Z.L. Evaluation of two end-member-based models for regional land surface evapotranspiration estimation from MODIS data. **Agricultural and Forest Meteorology**, v. 202, p. 69-82, 2015.

TAZEKRIT, I.; BENSLIMANE, M.; HAMIMED, A.; HARTA-NI, T.; KHALDI, A. Gestion concertée de l'eau des grands périmètres irrigués. Cas de la plaine de Habra (nord-ouest algérien). **Larhyss Journal**, n. 30, p. 121-136, 2017

TEIXEIRA, A.D.C.; BASTIAANSSEN, W.G.; AHMAD, M.U.D.; BOS, M.G. Reviewing SEBAL input parameters for assessing evapotranspiration and water productivity for the Low-Middle Sao Francisco River basin, Brazil: Part A: Calibration and validation. **Agricultural and Forest Meteorology**, v. 149, n. 3-4, p. 462-476, 2009.

TIMMERMANS, W.J.; KUSTAS, W.P.; ANDERSON, M.C.; FRENCH, A.N. An intercomparison of the surface energy balance algorithm for land (SEBAL) and the two-source energy balance (TSEB) modeling schemes. **Remote Sensing of Environment**, v. 108, n. 4, p. 369-384, 2007.

TREZZA, R.; ALLEN, R.G.; TASUMI, M. Estimation of actual evapotranspiration along the Middle Rio Grande of New Mexico using MODIS and landsat imagery with the METRIC model. **Remote Sensing**, v. 5, n. 10, p. 5397-5423, 2013.

WAGLE, P.; BHATTARAI, N.; GOWDA, P.H.; KAKANI, V.G. Performance of five surface energy balance models for estimating daily evapotranspiration in high biomass sorghum. **ISPRS Journal of Photogrammetry and Remote Sensing**, v. 128, p. 192-203, 2017.

YANG, Y. Remotely Sensed Evapotranspiration. In: **Observation and Measurement of Ecohydrological Processes**, LI, X.; VEREECKEN, H. (Eds.). Berlin Heidelberg: Springer, p. 155-200, 2019.

ZERKAOUI, L.; BENSLIMANE, M.; HAMIMED, A.; BETI-CHA, H. Adaptation du système d'irrigation dans les périmètres agricoles par modélisation du tour d'eau, cas de Habra (nord-ouest Algérien). **Agriculture and Forestry Journal**, v.1, n. 1, p. 1-9, 2017.

ZHANG, K.; KIMBALL, J.S.; RUNNING, S.W. A review of remote sensing based actual evapotranspiration estimation. **Wiley Interdisciplinary Reviews: Water**, v. 3, n. 6, p. 834-853, 2016.

ZHANG, Y.; ZHANG, L.; HOU, J.; GU, J.; HUANG, C. Development of an evapotranspiration data assimilation technique for streamflow estimates: A Case Study in a Semi-Arid Region. **Sustainability**, v. 9, n. 10, p. 1-21, 2017.

ZHU, W.; JIA, S.; LV, A. A Universal Ts-VI triangle method for the continuous retrieval of evaporative fraction from Modis products. **Journal of Geophysical Research: Atmospheres**, v. 122, n. 19, p. 10-206, 2017.

ZOU, M.; ZHONG, L.; MA, Y.; HU, Y.; HUANG, Z.; XU, K.; FENG, L. Comparison of two satellite-based evapotranspiration models of the Nagqu River Basin of the Tibetan Plateau. **Journal of Geophysical Research: Atmospheres**, v. 123, n. 8, p. 3961-3975, 2018.